Probabilistic Engineering Mechanics 81 (2025) 103777

Contents lists available at ScienceDirect

Probabilistic Engineering Mechanics

journal homepage: www.elsevier.com/locate/probengmech

Stochastic dispersion behavior and optimal design of locally resonant metamaterial nanobeams using nonlocal strain gradient theory

T. Chatterjee [a], S. El-Borgi [b], M. Trabelssi [c,d], M.I. Friswell [e,*]

[a] School of Engineering, University of Surrey, Guildford, GU2 7XH, UK
[b] College of Science and Engineering, Hamad Bin Khalifa University, Doha, Qatar
[c] Applied Mechanics and Systems Research Laboratory, Tunisia Polytechnic School, University of Carthage, B.P. 743, La Marsa, 2078, Tunisia
[d] Department of Mechanical Engineering, Tunis Higher National Engineering School, University of Tunis, 1008, Tunis, Tunisia
[e] Faculty of Science and Engineering, Swansea University, Swansea SA1 8EN, UK

ARTICLE INFO

Keywords:
Metamaterial nanobeam
Bandgap
Nonlocal strain gradient theory
Stochastic response analysis
Gaussian process modeling
Multi-objective optimization

ABSTRACT

This study examines the stochastic response of a metamaterial (MM) nanobeam, focusing on bandgap formation and analyzed using machine learning. The nanobeam is modeled as an infinitely long Euler–Bernoulli beam with two length scale parameters: the nonlocal and strain gradient parameter. Periodically distributed linear resonators along its length introduce periodicity. The deterministic analysis is conducted by estimating bandgap edge frequencies using the dispersion of elastic waves in a representative unit cell. The impact of uncertainties on wave propagation behavior indicate that geometric properties predominantly influence variability in frequency response, followed by material properties, affecting the location and width of the bandgap. Scale dependent parameters, however, have a negligible effect. A Gaussian process (GP) surrogate model is employed to efficiently capture the stochastic behavior of the nanobeam. To highlight the utility of machine learning in computationally intensive tasks, a multi-objective optimization problem is formulated to tailor the bandgap features of the nanobeam. The offline-trained GP model yields a Pareto front of design configurations closely aligned with actual simulations, eliminating the need for repeated analyses during optimization. This surrogate based optimizer efficiently facilitates reverse engineering of MM designs for user defined wave dispersion characteristics, showcasing its potential for large scale optimization. Importantly, the stochastic dispersion framework grounded in nonlocal strain gradient theory can be directly applied to other periodic MM nanostructures. By varying unit cell configurations and materials within the same computational pipeline, new insights into bandgap emergence across applications ranging from phononic waveguides, nanoscale acoustic devices to structure–property relationships in next-generation MMs can be rapidly obtained.

1. Introduction

In recent times, researchers have shown a keen interest in manipulating the elastic, acoustic, and electromagnetic properties of periodic structures known as phononic crystals or metamaterials, primarily due to their unique wave attenuation capabilities [1–7]. These structures possess frequency ranges within the band where mechanical waves are unable to travel, referred to as stop bands or bandgaps. The formation of these bandgaps occurs through two mechanisms: Bragg scattering (BS) and local resonance (LR).

The periodicity of these structures leads to high-frequency bandgaps through the Bragg scattering mechanism. The core frequency of these bandgaps is directly related to the wave velocity and the lattice constant of a typical unit cell [1]. On the other hand, the local resonance mechanism opens low-frequency stop bands, achieved by embedding multiple local resonators in the primary structure. These local resonators counteract the excitation of the input elastic wave, effectively attenuating the vibration of the main structure [2]. The core frequency of the stop bands in the local resonance mechanism is directly linked to the frequency of the resonator, necessitating the use of small-size periodic structures [3]. The applications of metamaterials have been extensive and diverse, encompassing noise and sound mitigation [1], structural vibration suppression [2], seismic protection [3], directional waveguides [4,5], mechanical filters [6], and electromagnetic stealth cloaks [7].

The utilization of metamaterials has, however, been predominantly confined to macro-structures, with limited exploration in the realm

* Corresponding author.
E-mail address: m.i.friswell@swansea.ac.uk (M.I. Friswell).

https://doi.org/10.1016/j.probengmech.2025.103777
Received 31 January 2025; Received in revised form 6 May 2025; Accepted 21 May 2025
Available online 6 June 2025

of nano-structures. Nevertheless, the demand for nanostructures has witnessed substantial growth in various applications over the last few decades due to their excellent mechanical, electrical, and thermal properties. Applications of nanostructures include actuators, sensors, microscopes, and micro/nano electro mechanical systems (MEMS/NEMS). Therefore, the application of metamaterials in nanostructures offers a promising avenue for research and development.

Nanostructures exhibit size-dependent behaviors that continuum mechanics struggles to account for. To overcome this limitation, nonclassical continuum theories have been developed, incorporating nonlocal, gradient elasticity, and couple stress theories. These theories are often preferred to molecular dynamics (MD) simulations which are, generally, computationally intensive, particularly when dealing with a large number of atoms. Nonlocal theories propose that the stress at a particular point within a body is influenced not only by the strain at that precise location but also by the strain throughout the entire domain [8–10]. These theories treat the body as particles influenced by long-range forces but do not account for microstructure deformation. These models are limited to nanostructures showing softening behavior [11–15]. On the other hand, the gradient elasticity theory stipulates that nanostructures can be modeled as assemblies of atoms with higher-order mechanical properties, and the total stress should include additional strain gradient terms [16–18]. However, this theory does not consider the effects of inter-atomic long-range forces. Gradient elasticity theory can only capture nanostructures exhibiting hardening behavior [11,19]. As a result, to model nanostructures demonstrating both hardening and softening behaviors, a combination of both theories is required. Such dual behavior was experimentally reported by Tian et al. [20]. In this context, Lim et al. [21] introduced a nonlocal strain gradient theory (NSG), which integrates the nonlocal and strain gradient theories into a unified framework. In this theory, the stress tensor incorporates contributions from both the nonlocal stress tensor and the strain gradient stress tensor. Since its inception, the NSG theory has been applied by several researchers to investigate the behavior of nanorods [11,22,23], nanobeams [24–28], and nanoplates [29–34].

The investigation of bandgap formation in metamaterial nanostructures has been undertaken by a limited number of researchers during the past few years. Qian et al. [35] employed the Plane Wave Expansion (PWE) method to analyze the band structure of a nonlinear Euler–Bernoulli nanobeam with piezoelectric properties, considering the nonlocal elasticity theory. Zhou et al. [36] developed and validated theoretical and numerical models to study the size-dependent formation of flexural wave bandgaps in a phononic crystal nanobeam, accounting for surface effects. The theoretical model employed the PWE method, while the numerical model utilized the spectral element method and the COMSOL Multiphysics finite element analysis software. Qian et al. [37] investigated the band structure of a Timoshenko nanobeam with piezoelectric properties, incorporating surface elasticity, and estimated the electro-mechanical bandgaps using the PWE method. In a subsequent study, Qian [38] utilized the PWE method to estimate the band structure of a piezoelectric nanobeam with Euler–Bernoulli properties, incorporating periodically spaced "spring–mass" resonators and considering surface effects. Qian and Wang [39] designed a novel resonator configuration to control the electro-mechanical coupling bandgap of phononic crystal nanobeams equipped with periodically spaced horizontal and vertical resonators. The band structure analysis of the proposed configuration was conducted using the PWE method. Espo et al. [40] addressed the estimation of bandgaps in a Timoshenko nanobeam with piezoelectric properties, considering surface effects and modified couple stress, employing the transfer matrix approach. Trabelssi et al. [41] investigated the formation of bandgaps in Euler–Bernoulli nanobeams using the nonlocal strain gradient theory. Through the use of Hamilton's principle, homogenization, and transfer matrix methods, the study derives and validates dispersion relations, conducting a parametric analysis to understand the effects of various parameters on bandgap formation in metamaterial nanobeams.

In addition, uncertainties are inevitable in architected micro or nanostructures and have the potential to cause pronounced manifestations of scale effects leading to variability in their vibration characteristics due to factors such as manufacturing imperfections, machining tolerances, material defects, surface roughness, environmental conditions and loading fluctuations [42]. The pioneering studies by Krishnan et al. [43] and Salvetat et al. [44] experimentally recorded significant variations in the elastic modulus and shear modulus of carbon nanotubes, clearly illustrating the inherent uncertainties and randomness present in nanostructural mechanics. An extensive investigation conducted by He et al. [45] studied the effect of defects on the mechanical properties of graphene sheets using molecular dynamics simulations and found significant influence on various parameters, including elastic modulus, tensile strength, and fracture behavior. These insights from the above early works focusing on inherent randomness in nanostructures provide valuable understanding of the effects of the presence of defects and measurement errors in structural mechanics and vibration behavior. More recent studies focusing on quantifying uncertainty in the context of the dynamics of nanostructures include, but are not limited to, specific applications in smart magneto-electro-elastic materials [46], carbon nanotube piezo nanocomposite [47], carbon nanotube reinforced functionally graded plates [48], nonlinear vibrations [49,50], polymeric nanocomposites [51], nanobeams combining first-order shear deformation theory with Eringen's nonlocal elasticity theory [52].

Furthermore, the following literature highlights that uncertainties have significantly influenced the wave propagation characteristics of elastic metamaterials. The manufacturing tolerances of metamaterial samples produced using a selective laser sintering method has been examined [53]. The random field model constructed from the observed spatial variability showed that even minor variations (i.e. less than 1% in the mass and less than 3% in the elastic modulus) significantly impact overall vibration attenuation performance. In fact, nano, micro, and macrostructures created via e-beam lithography, etching, and milling processes are especially prone to manufacturing uncertainties. It was observed that even optimized structures can suffer from diminished performance or, in extreme cases, complete loss of functionality due to tool wear, improper etching, or poorly calibrated e-beam equipment [54]. On the contrary, it has been noted that randomness or disorder can also improve the performance of metamaterials [55]. A stochastic finite element model for acoustic metamaterials was introduced in [56], utilizing a first-order Taylor series perturbation. Subsequently, Beli et al. [57] established an optimal threshold for disorder, below which the attenuation bandwidth expands, while higher disorder levels result in the mistuning of the bandgap, negating the overall attenuation. Investigations into the impact of uncertainties on dispersion at both the unit-cell and finite metamaterial levels have been conducted, and an approach to achieve desired bandgap characteristics proposed [58]. A sensitivity analysis of the random geometric parameters such as plate thickness, resonator radius, and resonator length was carried out on bandgap properties using a spectral method based on generalized polynomial chaos [59]. Additionally, the approximation of closely spaced modes in periodic structures, focusing on mode degeneration under uncertainty was explored [60]. Recently, novel machine learning (ML) based computational frameworks for generalized uncertainty quantification (UQ) were proposed to investigate stochastic wave propagation in various applications, including 2D hexagonal lattices [61], the stochastic Hofstadter butterfly spectrum and edge states in 1D inerter-based quasi-periodic lattices [62], and the phenomenon of stochastic metadamping in active acoustic metamaterials [63].

All of the findings from the literature stated in the previous two paragraphs highlight the limitations of conventional deterministic approaches to effectively capture the possible random scenarios and reinforce the need for UQ in analyzing vibration characteristics of nanobeam metamaterials. Therefore, accurate modeling of potential uncertainties and prediction of the stochastic dynamic behavior at the

pre-design/conceptual stage is crucial to achieve a fundamental understanding of the underlying physics, ensuring their targeted functionality via resilient, reliable design and leading to improved performance by suitably informing the design optimization process [64]. To this end, a systematic investigation has been carried out in this work to examine the effect of material, geometric and scale-dependent parametric randomness at the unit cell level on the wave propagation characteristics in locally resonant metamaterial nanobeams modeled using nonlocal strain gradient theory. A supervised machine learning technique, the Gaussian process (GP), has been trained to serve as the computationally efficient predictive surrogate model to capture the stochastic dispersion response of the metamaterial nanobeam. To further assess the effectiveness of the GP model, a multi-objective optimal (inverse) design of the metamaterial nanobeam has been performed based on desirable dispersion (bandgap) characteristics.

To the best of the authors' knowledge, this is the first work combining ML based UQ and optimal design based on the wave propagation in locally resonant metamaterial nanobeams modeled using nonlocal strain gradient theory. Although this study focuses on nanobeam-based elastic metamaterials, the proposed framework is modular and applicable to various other nanoscale configurations. The modeling approach accommodates size-dependent phenomena through nonlocal and strain gradient effects, which are particularly relevant for nanostructures. Furthermore, the ML and optimization components are agnostic to specific techniques, allowing users to integrate alternative surrogates or solvers as per problem-specific requirements. This end-to-end adaptability makes the framework a practical tool for rapidly mapping bandgap formation across a broad spectrum of next-generation metamaterials.

The paper is arranged as follows. Following this introduction, Section 2 describes the derivation and normalization of the equations of motion of a nonlocal strain gradient metamaterial nanobeam based on Hamilton's principle. Section 3 is dedicated to the derivation of the dispersion equation based on the homogenization approach. The stochastic modeling framework using machine learning is given in Section 4. The numerical investigation of the stochastic framework and multi-objective optimization are presented in Section 5. A summary of this study and concluding remarks are provided in Section 6.

2. Wave propagation and bandgap formation in a beam with local resonators

The analysis begins by considering the bending behavior of an isolated uniform beam. The beam structure is defined in a Cartesian coordinate system (x, z) where x is the longitudinal axis along the neutral axis of the beam, and z is the vertical axis. The governing equation is the classical Euler–Bernoulli beam equation, a fourth-order partial differential equation (PDE) describing transverse motion:

$$EI\frac{\partial^4 w(x,t)}{\partial x^4} + \rho A\frac{\partial^2 w(x,t)}{\partial t^2} = 0 \tag{1}$$

where t is the time variable, E is the Young's modulus, I is the second moment of area, ρ is the mass density, A is the cross-sectional area, and $w(x,t)$ is the displacement of the neutral axis of the beam along the transverse direction z. Assume a harmonic wave solution of the form

$$w(x,t) = We^{i(kx-\omega t)} \tag{2}$$

where $i = \sqrt{-1}$ is the imaginary unit, k is the Bloch wave number, ω is the angular frequency, and W is the motion amplitude of the beam. Substituting the above assumed solution into the PDE yields the following dispersion relation:

$$\omega^2 = \frac{EI}{\rho A}k^4 \tag{3}$$

Thus, the angular frequency ω scales quadratically with the wavenumber k, and the phase velocity v_p, defined as

$$v_p = \frac{\omega}{k} \tag{4}$$

varies with k. Even though the beam is non-periodic, dispersion naturally arises because different wavelength components travel at different speeds during beam bending due to the fourth-order nature of the governing PDE. Fig. 1a shows the so-called dispersion relation for the Euler–Bernoulli beam flexural waves, which is a plot of the frequency versus wave number. Additional details can be found in Chapter 8 of the book by Kim [65].

Local resonators are introduced periodically along an infinitely long beam to investigate the influence of periodic attachments, as shown in Fig. 2. Each resonator is modeled as a single-degree-of-freedom linear spring–mass system with mass m_r, spring stiffness k_r, and its corresponding natural frequency ω_r. When a resonator is attached, the dynamic response of the beam–resonator system changes significantly compared to the bare beam. Multiple methods can derive the dispersion relation for the beam with periodically attached resonators. One classical approach is to apply Bloch–Floquet theory to the unit cell, wherein the displacement field satisfies the following periodicity condition:

$$w(x+a,t) = e^{ika}w(x,t) \tag{5}$$

where a is the periodic length. The transfer matrix method enforces the continuity of displacement, slope, moment and shear force between the unit cells, and Bloch–Floquet enforces periodicity. Alternatively, a homogenization approach may be employed, wherein the periodic system is approximated by an equivalent continuous medium with effective mass and stiffness properties that vary with frequency. Under this framework, the governing equations are modified to account for the dynamic influence of the resonators, leading to a frequency-dependent effective model. Regardless of the method employed, whether direct Bloch analysis or homogenization, the formulation ultimately reduces to an eigenvalue problem, wherein the admissible frequencies ω are determined as functions of the wavenumber k. Solving the eigenvalue problem reveals the presence of two distinct dispersion branches separated by a bandgap, the characteristics of which depend on the resonator parameters, particularly the resonator mass, and stiffness. If two dispersion curves remain non-intersecting, a discontinuity emerges along the ω axis, delineating a frequency range wherein wave propagation is inhibited, commonly referred to as a bandgap (BG), as illustrated in Fig. 1b. The bandgap thus identifies frequency intervals over which wave motion is restricted. In contrast, the regions along the wavenumber axis that coincide with the dispersion branches define the pass band (PB), within which wave propagation is permitted.

A comparative study is conducted between two cases: the bare beam and the beam equipped with periodic resonators. For the bare beam, the dispersion curve remains continuous, indicative of classical flexural wave propagation, as shown in Fig. 1b. However, with the inclusion of resonators, significant scattering occurs near the resonator frequency, resulting in discontinuities in the dispersion relation, as shown in Fig. 1b. These discontinuities correspond to frequency ranges where no real ω solutions exist for all k values, thus defining the bandgap where wave propagation is inhibited. This framework captures the essential mechanisms governing bandgap formation through local resonators attached to continuous beams.

3. Equations of motion of the nonlocal strain gradient metamaterial nanobeam

The nonlocal strain gradient theory proposed by [21,66] stipulates that the total stress tensor $\mathbf{t}$ considers both the nonlocal stress tensor σ and the higher-order strain gradient nonlocal stress tensor $\nabla\sigma^{(1)}$, where $\sigma^{(1)}$ is the higher-order nonlocal stress tensor. In other words, the total stress at a given point $\mathbf{x}$ depends not only on the strain ϵ and its gradient at that point but on the strains and their corresponding gradients at all other points within a given domain V. A simplified differential form of the constitutive equations is generally used:

$$\mathbf{t} = \sigma - \nabla\sigma^{(1)} \tag{6a}$$

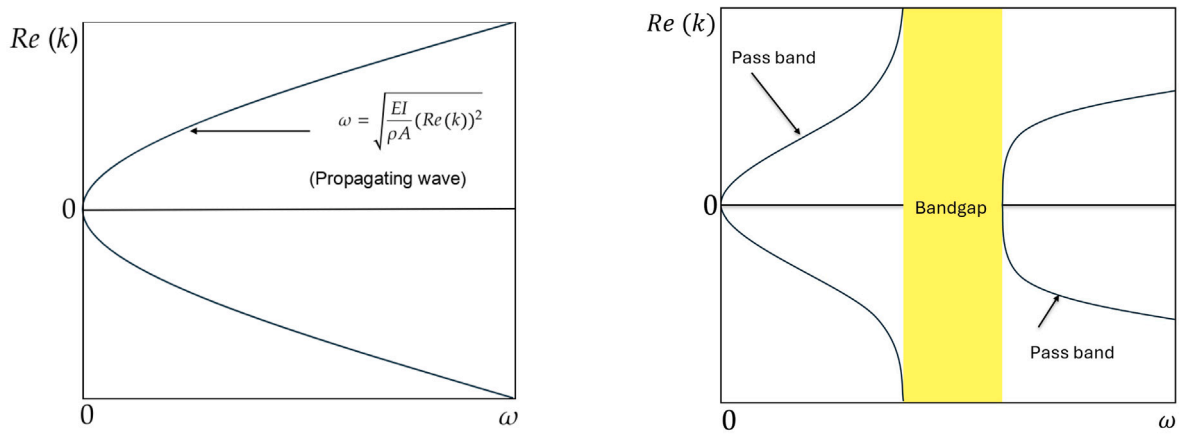

(a) Beam without resonators.

(b) Beam equipped with periodically distributed local resonators.

Fig. 1. Dispersion relation ($\omega - k$ relation) for flexural waves in an Euler–Bernoulli beam with and without resonators.

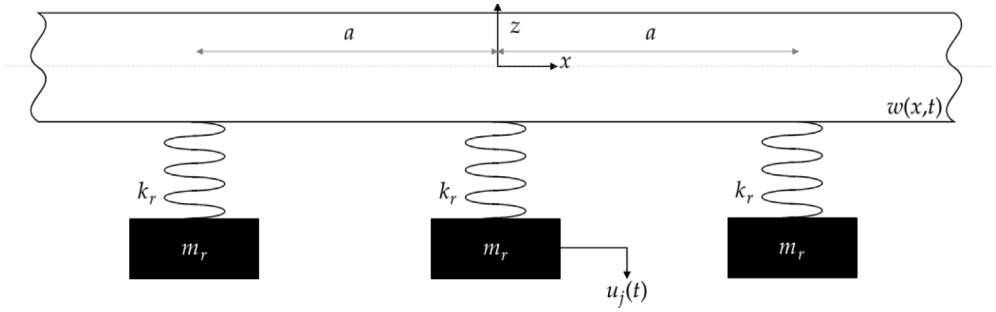

Fig. 2. Schematic of an infinitely long metamaterial Euler–Bernoulli beam/nanobeam equipped with periodically distributed load resonators.

$$\left(1-\mu_0^2\nabla^2\right)\boldsymbol{\sigma} = \mathbf{C}:\boldsymbol{\varepsilon} \tag{6b}$$

$$\left(1-\mu_0^2\nabla^2\right)\boldsymbol{\sigma}^{(1)} = l_s^2\mathbf{C}:\nabla\boldsymbol{\varepsilon}\mathbf{t} = \sigma - \nabla\sigma^{(1)} \tag{6c}$$

in which ε is the classical strain tensor, $\mathbf{C}$ is the fourth-order elasticity tensor, l_s is the strain gradient length-scale parameter and μ_0 is the nonlocal parameter. ∇^2 is the Laplacian operator. Substituting (6b) and (6c) into (6a) gives

$$\left(1-\mu_0^2\nabla^2\right)\mathbf{t} = \left(1-l_s^2\nabla^2\right)\mathbf{C}:\boldsymbol{\varepsilon} \tag{7}$$

Furthermore, for a beam-type structure defined in a Cartesian coordinate system (x, z) where x is the longitudinal axis along the neutral axis of the beam and z is the vertical axis, it is assumed that the size-dependency is only accounted for in the longitudinal direction and neglected in the other directions. Therefore, Eq. (7) can be reduced to the following:

$$\left(1-\mu_0^2\frac{\partial^2}{\partial x^2}\right)t_{xx} = \left(1-l_s^2\frac{\partial^2}{\partial x^2}\right)E\varepsilon_{xx} \tag{8}$$

where ∇^2 was replaced by $\partial^2/\partial x^2$ and E is the elastic modulus of the nanobeam.

Consider an infinitely long beam with elastic modulus E, density ρ, cross-sectional area A. Attached to the nanobeam is a set of periodically distributed linear resonators, as shown in Fig. 2. Each resonator is modeled as a single-degree-of-freedom linear spring–mass system with mass m_r and spring stiffness k_r. According to linear Euler–Bernoulli Beam Theory, the components of the displacement field along the x and z coordinates can be written as [67]

$$u_x(x,z,t) = -zw^{(1,0)}(x,t) \tag{9a}$$

$$u_z(x,z,t) = w(x,t) \tag{9b}$$

where $w(x,t)$ is the displacement of the neutral axis of the nanobeam along the transverse direction z. The beam rotation $w^{(1,0)}(x,t)$ follows the partial derivative definition:

$$\frac{\partial^{n+m}}{\partial x^n\partial t^m}w(x,t) = w^{(n,m)}(x,t)$$

The Euler–Bernoulli Beam Theory (EBT) and the Nonlocal Strain Gradient Theory (NSGT) are used to model the nanobeam. Applying Hamilton's principle to the nanobeam yields [41]

$$m\left(1-\mu_0^2\partial_x^2\right)w^{(0,2)} + EI\left(w^{(4,0)} - l_s^2w^{(6,0)}\right) + \sum_{j=1}^{n} m_r\left(w^{(0,2)}|_{x_j,t} + y_j''\right)\bar{\delta}_{x_k} = 0 \tag{10a}$$

$$m_r\left(w^{(0,2)}|_{x_j,t} + y_j''\right) + k_r y_j = 0 \quad j = 1,\ldots,n \tag{10b}$$

in which $m = \rho A$ is the mass per unit length of the nanobeam, u_j and y_j are, respectively, the absolute displacement and the elongation of the spring of the jth resonator in x_j, that is, $y_j = u_j - w|_{x_j}$. $\bar{\delta}_{x_k}(x)$ is the translated Dirac function, and y_j'' is the second derivative of y_j with respect to time t which is denoted as

$$y_j'' = \frac{d^2y_j}{dt^2}$$

The following non-dimensional parameters are now introduced:

$$\omega_c = \frac{1}{a^2}\sqrt{\frac{EI}{m}},\ \omega_r = \sqrt{\frac{k_r}{m_r}},\ \tilde{\omega}_r = \frac{\omega_r}{\omega_c}$$

$$\xi = \frac{x}{a},\ \tau = t\omega_c,\ v = \frac{w}{a},\ q = \frac{y}{a},\ \mu_r = \frac{m_r}{am},\ \bar{l}_s = \frac{l_s}{a},\ \bar{\mu}_0 = \frac{\mu_0}{a} \tag{11}$$

The non-dimensional governing equations of motion of the NSGT metamaterial nanobeam can, therefore, be written as

$$\left(1-\bar{\mu}_0^2\partial_\xi^2\right)v^{(0,2)} + v^{(4,0)} - \bar{l}_s^2v^{(6,0)} + \sum_{j=1}^{n}\left(\mu_r v^{(0,2)}|_{\xi_j,\tau} + \mu_r q_j''\right)\bar{\delta}_{\xi_k} = 0 \tag{12a}$$

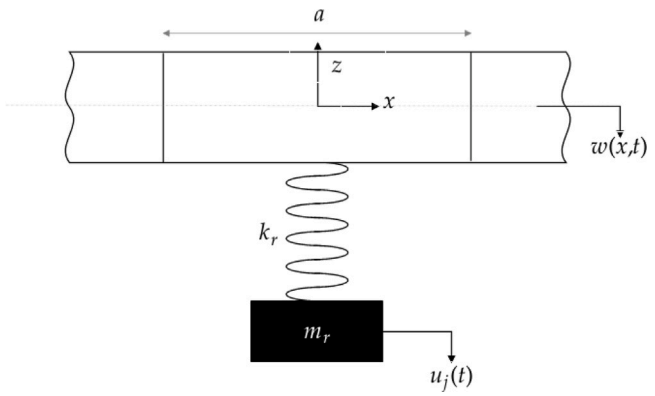

Fig. 3. Schematic of the unit cell used in the homogenization method.

$$v^{(0,2)}\,|_{\xi_j,\tau} + q_j'' + \tilde{\omega}_r^2 q_j = 0 \qquad j = 1,\ldots,n \tag{12b}$$

where ω_r is the resonator natural frequency, μ_r is the resonator beam mass ratio, ω_c is a time re-scaling parameter, $\bar{l}_s$ is the normalized SGT length scale parameter, $\tilde{\omega}_r$ is the dimensionless resonator frequency and $\bar{\mu}_0$ is the normalized nonlocal length-scale parameter. In addition, q_j'' is the second derivative of q_j with respect to the dimensionless time τ which is denoted as

$$q_j'' = \frac{d^2 q_j}{d\tau^2}$$

4. Bandgap formation analysis

When the length of the beam is very long relative to the spacing of the periodic resonators, several mode shapes must be included in the analysis, thereby making the computational cost prohibitively expensive. Therefore, it may be convenient to assume that the beam is infinitely long and that the attached resonators are periodically distributed with a constant lattice spacing. In light of this assumption, the beam may be divided into an infinite number of periodic unit cells and its dynamic behavior analyzed by taking advantage of the periodicity of the boundary conditions of a single repeated unit cell. In other words, as discrete modes do not exist and the motion of the beam can be analyzed through the propagation of an elastic wave in a representative periodic unit cell of the infinite structure [68]. Different methods have been employed to study the bandgap formation in an infinite locally resonant beam, such as the Transfer Matrix (TM) method [69–71], Spectral Element Method (SEM) [72,73], homogenization method [74,75]. In this study, we consider the homogenization method only.

The nanobeam can be divided into several cells, with a single resonator in each unit cell. The resonator is located at the origin of the coordinate system of the unit cell, i.e. at $x = 0$ as shown in Fig. 3. The origin of the coordinate system of the unit cell is placed at the center of the cell j.

The nanobeam may be treated as a homogenized uniform beam by integrating the equation of motion (12a) over the normalized length of the unit cell

$$\int_{\frac{-1}{2}}^{\frac{1}{2}} \left[\left(1 - \bar{\mu}_0^2 \partial_\xi^2\right) v^{(0,2)} + v^{(4,0)} - \bar{l}_s^2 v^{(6,0)}\right] d\xi + \mu_r \left(v^{(0,2)}\,|_{0,\tau} + q_j''\right) = 0 \tag{13}$$

An elastic wave propagating through the cell can be assumed to have a harmonic solution of the form

$$v(\xi,\tau) = \underline{v}(\tau) e^{i\lambda\xi} \tag{14}$$

where $\underline{v}(\tau)$ is the amplitude of the representative beam element and λ denotes the wave number. Substituting the above solution into Eq. (13) gives

$$\mu_r q_j''(\tau) + (\mu_r + \bar{m})\underline{v}''(\tau) + \bar{k}\underline{v}(\tau) = 0 \tag{15a}$$

$$q_j''(\tau) + \underline{v}''(\tau) + \tilde{\omega}_r^2 q_j(\tau) = 0 \tag{15b}$$

where

$$\bar{m} = \frac{2}{\lambda}\sin\left(\frac{\lambda}{2}\right)\left(1 + \lambda^2\bar{\mu}_0^2\right), \qquad \bar{k} = 2\lambda^3 \sin\left(\frac{\lambda}{2}\right)\left(\lambda^2\bar{l}_s^2 + 1\right) \tag{16}$$

In addition, $\underline{v}(\tau)$ and $q_j(\tau)$ are assumed to be harmonic, so that

$$\underline{v}(\tau) = \mathcal{V} e^{i\tau\Omega}, \qquad q_j(\tau) = \mathcal{Q}_j e^{i\tau\Omega}$$

where Ω is the dimensionless frequency of the wave and $\mathcal{V}$ and $\mathcal{Q}_j$ are the amplitudes of $\underline{v}$ and q_j, respectively. Substituting the above solutions into Eqs. (15)(a,b) yields the following system of equations, written in a matrix form:

$$\begin{pmatrix} \bar{k} - (\mu + \bar{m})\Omega^2 & -\mu\Omega^2 \\ -\Omega^2 & \tilde{\omega}_r^2 - \Omega^2 \end{pmatrix} \begin{Bmatrix} \mathcal{V} \\ \mathcal{Q}_j \end{Bmatrix} = \begin{Bmatrix} 0 \\ 0 \end{Bmatrix} \tag{17}$$

The determinant of the above linear system of equations must vanish to avoid a non-trivial solution resulting in the following dispersion equation:

$$\bar{k}\left(\tilde{\omega}_r^2 - \Omega^2\right) - \mu\Omega^4 + (\mu + \bar{m})\left(\Omega^4 - \Omega^2\tilde{\omega}_r^2\right) = 0 \tag{18}$$

5. Stochastic modeling using machine learning

5.1. General computational framework

In a physical system governed by a set of equations, such as differential equations, the general input–output relationship of the model can be represented as

$$\mathbf{y} = \mathbf{M}(\mathbf{x}) \tag{19}$$

where $\mathbf{x} \in \mathbb{R}^M$ is a vector of input parameters that define the geometrical details, material properties, and loading conditions, and $\mathbf{y} \in \mathbb{R}^Q$ represents the vector of mechanical response quantities of interest, which may include:

- Displacement response or related components
- Natural frequencies, modal contribution factors, and other eigenspace response components
- Strain and stress tensor components at specific locations
- Plastic strain and other metrics measuring internal damage
- Spatial and temporal evolution of these quantities

Our objective is to establish a generalized non-intrusive framework for stochastic modeling, considering the computational model **M** as a black box. This means that the model configuration settings are fixed and cannot be modified by the user, providing unique response values for each input vector combination. Since **M** is deterministic, repeating the analysis with the same set of input parameters will yield identical output response values each time. Stochastic input parameters are modeled by random realizations of the vector $\mathbf{x} \in \mathbb{R}^M$ according to a specified probability density function $f_x(\mathbf{x})$. Conventional techniques often use statistical inference approaches, such as the maximum likelihood estimate and criteria like Akaike and Bayesian information to select the best-fit distribution [76,77]. Alternatively, Bayesian statistics can be employed to enhance model predictions by incorporating measurement data alongside system physics, and the maximum entropy approach is useful when data is scarce or unavailable.

5.2. Context to wave dispersion of nanobeam metamaterial

When system uncertainties are incorporated, the deterministic wave dispersion response based on the homogenization unit cell approach, Eq. (18), transforms into a stochastic problem, resulting in a random dispersion relation. A straightforward way to handle such a stochastic problem is to compute the dynamic response of the nanobeam metamaterial for each realization of random input parameters. This approach, known as crude Monte Carlo simulation (MCS), involves conducting a large number of simulations on the actual system, for example solving an eigenvalue problem for thousands of stochastic input realizations. This process can be computationally intensive, particularly for the wave dispersion response of metamaterials (as previously stated) where it is necessary to solve the resulting dispersion relation using the homogenization unit cell approach, Eq. (18), corresponding to each stochastic input realization. Therefore, to reduce the associated computational cost of physics-based solvers, surrogate modeling via ML has been performed. Specifically, the ML technique known as the Gaussian process (GP) has been employed as a gray-box model to emulate the stochastic dynamic behavior of the nanobeam metamaterial. Subsequently, the (offline) trained GP model can accelerate the prediction of the wave dispersion relation on unseen/new data and hence, can be readily employed for more computationally demanding online tasks (which are repeated over multiple iterations) such as, design optimization and multi-criterion decision making.

5.3. Gaussian process formulation

This section presents the mathematical formulation of GP. Originally introduced as a spatial interpolation method in the field of geostatistics, GP is a stochastic process that establishes probabilistic distributions over functions [78]. Its application has since broadened to encompass various fields, including structural dynamics [79]. A GP over the function $g(\mathbf{x})$ (where, $g : \mathbb{R}^d \rightarrow \mathbb{R}$) with mean $\mu(\mathbf{x})$ and covariance function $\kappa(\mathbf{x}, \mathbf{x}'; \Theta)$ can be expressed as follows:

$$\begin{aligned} g(\mathbf{x}) &\sim GP(\mu(\mathbf{x}), \kappa(\mathbf{x}, \mathbf{x}'; \Theta)), \\ \mu(\mathbf{x}) &= \mathbb{E}[g(\mathbf{x})] \\ \kappa(\mathbf{x}, \mathbf{x}'; \Theta) &= \mathbb{E}[(g(\mathbf{x}) - \mu(\mathbf{x}))(g(\mathbf{x}') - \mu(\mathbf{x}'))] \end{aligned} \tag{20}$$

where, $\mathbf{x} \in \mathbb{R}^d$ represents the independent variable and Θ represents the hyperparameters of the covariance function κ. By choosing an appropriate covariance function κ, it is possible to incorporate any relevant prior knowledge about the function $g(\mathbf{x})$ being modeled, for example its linearity, or smoothness. Therefore, this enhances the approximation accuracy by effectively capturing the complex functional trends. Additionally, the covariance function defines the relationships between the function values evaluated at different input points.

It is important to note that, unlike traditional modeling methods that employ a parameterized mathematical function to describe the input–output relationship, a GP does not depend on an explicit form. Instead, it uses a prior belief expressed through the mean and covariance functions over the space of potential response functions [76]. This characteristic classifies GPs as non-parametric models.

In this study, we have utilized up to the second-order polynomial terms in the trend component of GP (also known as Universal Kriging) [80], which can be expressed as

$$\mathbf{y}(\mathbf{x}) = \sum_{j=1}^{p} \beta_j \mathbf{f}_j(\mathbf{x}) + \mathbf{z}(\mathbf{x}) \tag{21}$$

where $\boldsymbol{\beta} = \{\beta_j, j = 1, \ldots, p\}$ and $\mathbf{F} = \{\mathbf{f}_j, j = 1, \ldots, p\}$ represent the vector of unknown coefficients and the polynomial basis matrix, respectively. The GP, expressed by $\mathbf{z}(\mathbf{x})$ has a zero mean and an autovariance given by $\text{cov}[\mathbf{z}(\mathbf{x}), \mathbf{z}(\mathbf{x}')] = \sigma^2 \mathbf{R}(\boldsymbol{\theta}, \mathbf{x}, \mathbf{x}')$, where σ^2 and $\mathbf{R}(\boldsymbol{\theta}, \mathbf{x}, \mathbf{x}')$ are the process variance and the autocorrelation function with parameters $\boldsymbol{\theta}$, respectively. In this study, various well-known stationary correlation functions have been employed for quantitative analysis (see Appendix for details).

Assuming the noise $\mathbf{z} = \mathbf{y} - \mathbf{F}\boldsymbol{\beta}$ forms a correlated Gaussian vector, the parameters $\boldsymbol{\beta}$ and σ^2 can be determined using the maximum likelihood estimate approach, which involves solving the following optimization problem.

$$\begin{aligned} (\hat{\boldsymbol{\beta}}, \hat{\sigma}^2) &= \arg\max_{\boldsymbol{\beta}, \sigma^2} \mathbf{L}(\boldsymbol{\beta}, \sigma^2 | \mathbf{y}) \\ &= \frac{1}{((2\pi\sigma^2)^n \det\mathbf{R})^2} \exp\left[-\frac{1}{2\sigma^2}(\mathbf{y} - \mathbf{F}\boldsymbol{\beta})^T \mathbf{R}^{-1}(\mathbf{y} - \mathbf{F}\boldsymbol{\beta})\right] \end{aligned} \tag{22}$$

Eq. (22) yields the estimates $(\hat{\boldsymbol{\beta}}, \hat{\sigma}^2)$ as

$$\hat{\boldsymbol{\beta}} = (\mathbf{F}^T \mathbf{R}^{-1} \mathbf{F})^{-1} \mathbf{F}^T \mathbf{R}^{-1} \mathbf{y} \tag{23}$$

$$\hat{\sigma}^2 = \frac{1}{n}(\mathbf{y} - \mathbf{F}\boldsymbol{\beta})^T \mathbf{R}^{-1}(\mathbf{y} - \mathbf{F}\boldsymbol{\beta}) \tag{24}$$

where the model response is given by $\mathbf{y} = \{y_1, \ldots, y_n\}^T$.

To generate a prediction response for a test point using GP, three conditions need to be satisfied: linearity with respect to the observed data, unbiasedness, and minimal variance. The predicted mean and variance of the GP can be expressed as follows:

$$\mu_{\hat{Y}}(\mathbf{x}) = \mathbf{F}^T \hat{\boldsymbol{\beta}} + \mathbf{r}^T \mathbf{R}^{-1}(\mathbf{y} - \mathbf{F}\hat{\boldsymbol{\beta}}) \tag{25}$$

$$\sigma^2_{\hat{Y}}(\mathbf{x}) = \hat{\sigma^2}[1 - \mathbf{r}^T \mathbf{R}^{-1} \mathbf{r} + \mathbf{u}^T (\mathbf{F}^T \mathbf{R}^{-1} \mathbf{F})^{-1} \mathbf{u}] \tag{26}$$

where $\mathbf{u} = \mathbf{F}^T \mathbf{R}^{-1} \mathbf{r} - \mathbf{R}$ and $\mathbf{r}$ represent the autocorrelation between the unknown point $\mathbf{x}$ and each point of the observed data set.

The formulation described above has several notable attributes: (i) it provides exact prediction values at the training points, with a variance of zero at these locations, (ii) as the size of the observed data set increases, the variance asymptotically converges to zero, and (iii) a prediction at a given point is treated as a realization of a Gaussian random variable, enabling the determination of confidence intervals for the prediction. The variance information is often used to quantify the epistemic uncertainty in the meta-model due to data sparsity, and has inspired adaptive architectures to further enhance approximation accuracy [81–83].

6. Results and discussion

6.1. Stochastic analysis

Stochastic response analysis has been carried out by considering variability in the material, geometric and non-classical continuum model parameters at the unit cell level of the locally resonant metamaterial nanobeam. The material parameters, elastic modulus (E) and density (ρ), the geometric parameters, radius (r) and unit cell length (a) and the resonator stiffness (k_r) are considered to be random following lognormal distribution with 5% variation. The nonlocal and strain gradient parameters are considered to be random following uniform distribution with their mean values as $3a$ and $1.5a$, respectively and 5% variation. Hence, the resulting bounds of the nonlocal and strain gradient parameters are: $[2.74a \;\; 3.26a]$ and $[1.37a \;\; 1.63a]$, respectively. The mean values of the parameters following the lognormal distribution are considered to be the same as their nominal values adopted in [41], unless otherwise mentioned with the radius $r = 0.5 \times 10^{-9}$ m, unit cell length $a = 20r$, elastic modulus $E = 70$ GPa, $\rho = 2600\,\text{kg/m}^3$, resonator stiffness $k_r = (2\pi \times 10^8)^2\, m_r$ N/m, where m_r is the resonator mass. Note that m_r is fixed based on a constant resonator to unit cell mass ratio of $\mu_r = 0.4$.

The above assumption of lognormal distribution has been primarily based on the existing literature which indicates that it is one of a number of suitable distributions to model properties which are inherently positive and exhibit variability proportional to their mean (for example, in strength related parameters), the others being Weibull and normal

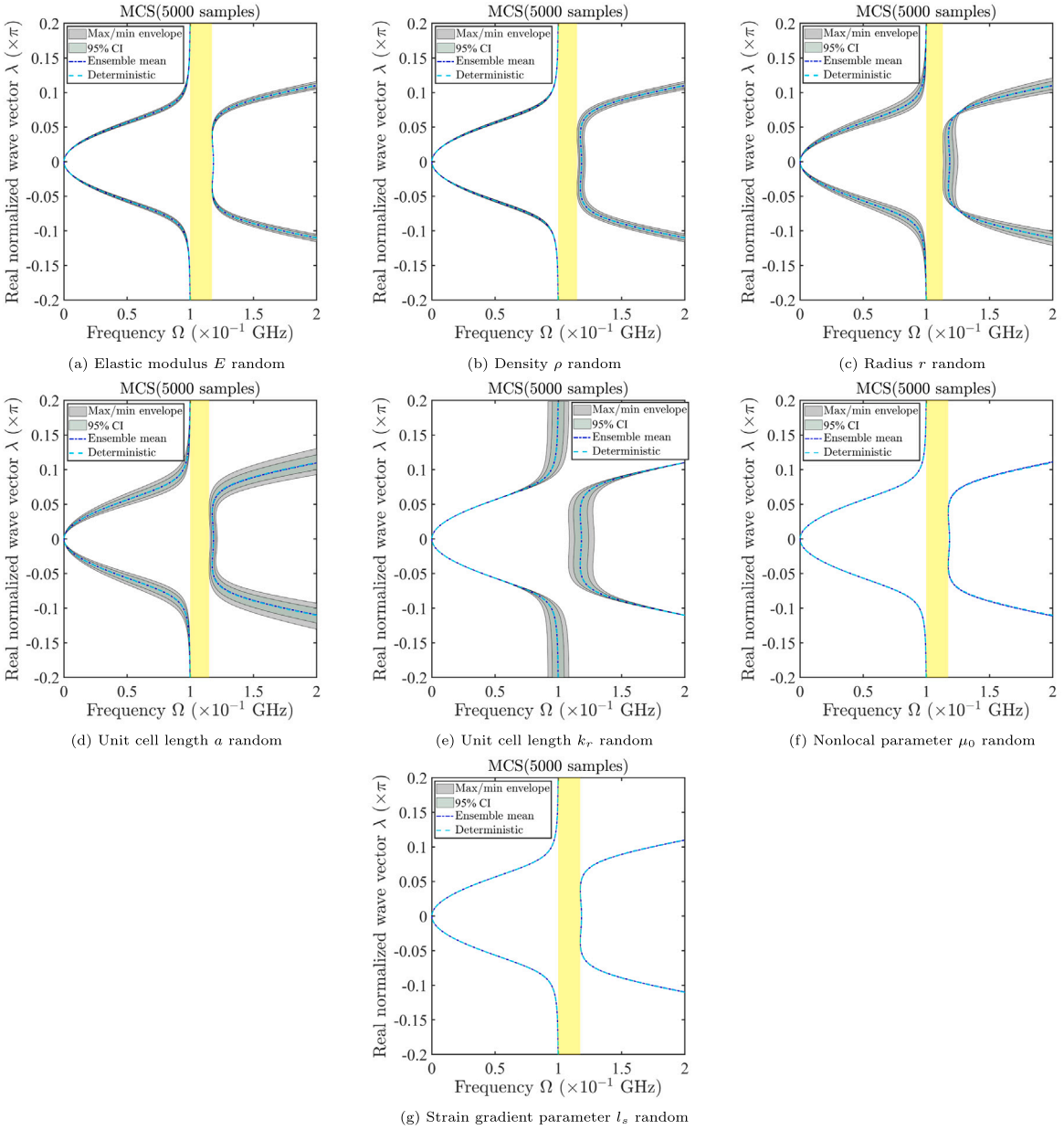

(a) Elastic modulus E random (b) Density ρ random (c) Radius r random

(d) Unit cell length a random (e) Unit cell length k_r random (f) Nonlocal parameter μ_0 random

(g) Strain gradient parameter l_s random

Fig. 4. Stochastic dispersion plots with the bandgap indicated in yellow obtained using MCS (5000 samples). The wave dispersion responses have been obtained by considering the individual system parameters, (a) Elastic modulus E (b) Density ρ (c) Radius r (d) Unit cell length a (e) Resonator stiffness k_r (f) Nonlocal parameter μ_0 and (g) Strain gradient parameter l_s as random. (For interpretation of the references to color in this figure legend, the reader is referred to the web version of this article.)

distributions [84]. The assumption of uniform distribution for the scale dependent parameters was based on the absence of an obvious candidate due to insufficient literature. Therefore, it was selected to provide equal weight to all outcomes within a given range (as commonly found in manufacturing tolerances). However, the ML-based stochastic wave propagation framework employed here is generalized and is able to deal with all possible probabilistic distributions.

At first, a parametric study has been conducted to investigate the effect of individual stochastic parameters on the bandgap characteristics. The results of this study have been presented in the form of wave dispersion plots in Fig. 4. Furthermore, in order to quantitatively assess the stochastic effect of individual parameters on the wave dispersion response, the mean and the coefficient of variation (C.o.V.) of the bandgap center and bandgap width have been reported in Table 1. The bandgap center and bandgap width have been evaluated as,

$$\text{Bandgap center} = (\omega_u + \omega_l)/2 \tag{27}$$

$$\text{Bandgap width} = \omega_u - \omega_l \tag{28}$$

The statistics reported in Table 1 reveal that the geometric properties followed by the material properties emerge as the most influential parameters leading to the most significant change in the frequency response, and consequently in the bandgap parameters. It is also clear that the scale dependent parameters cause insignificant change in the frequency and bandgap characteristics. The above information on the sensitivity of the system parameters is crucial for informed decision making in engineering design and optimization of the nanobeam metamaterial. In general, it is observed that the bandgap width is more sensitive than the bandgap center which is relatively stable as indicated by their respective C.o.V values. This observation on higher variability in the bandgap width emphasizes the need to consider uncertainties for the effective targeted design of wave filters. Through such a robust

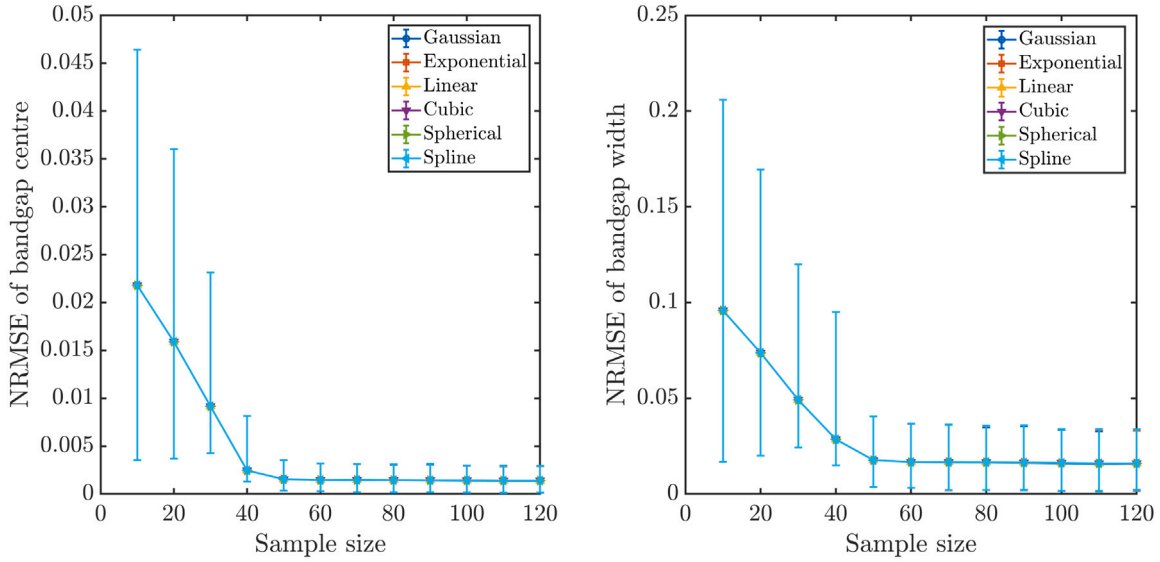

(a) Error convergence of the bandgap centre

(b) Error convergence of the bandgap width

Fig. 5. Convergence of the normalized root mean squared error with training sample size for various covariance functions of the GP model in approximating the (a) bandgap center and (b) bandgap width. Note that the error bars have been obtained corresponding to the GP models trained on 50 different pseudo random seeds with the symbols representing the mean error values for the same covariance function.

Table 1
Comparison of the statistics of bandgap center and bandgap width obtained corresponding to various stochastic configurations. For the deterministic system configuration, the bandgap center is 1.0858 and bandgap width is 0.1749 ($\times$ 10^{-1} GHz).

Random quantities	Bandgap center ($\times 10^{-1}$ GHz)		Bandgap width ($\times 10^{-1}$ GHz)	
	Mean	C.o.V.	Mean	C.o.V
Elastic modulus E	1.0857	2.3804×10^{-4}	0.1749	0.002
Density ρ	1.0860	0.0038	0.1754	0.0467
Radius r	1.0863	0.0066	0.1760	0.0853
Unit cell length a	1.0860	0.0037	0.1754	0.0423
Resonator stiffness k_r	1.0850	0.0243	0.1748	0.0226
Nonlocal parameter μ_0	1.0853	2.1484×10^{-14}	0.1740	2.7923×10^{-14}
Strain gradient parameter l_s	1.0858	2.0043×10^{-14}	0.1748	1.5717×10^{-14}
All the above combined	1.0864	0.0265	0.1772	0.1101

design of metamaterials, a specific stop band region covering a certain range of frequencies can be achieved, thereby unlocking the full potential of their functionalities.

Gaussian process (GP) has been utilized as the ML model to train and predict the stochastic wave response of the locally resonant nanobeam metamaterial. The MATLAB-based DACE platform has been employed to implement the GP model [80]. Up to second-order polynomial basis (i.e., Universal Kriging) has been used to train the GP. The Latin hypercube sampling (LHS) scheme has been implemented to train the GP model via the built-in function 'lhsdesign' in MATLAB. For benchmarking purposes, the predictions obtained using GP have been validated by performing Monte Carlo simulations (MCS). For a fair assessment of the predictive accuracy, the trained GP model has been tested using the same dataset as utilized for reporting the MCS results. For quantitative assessment of the predictive test accuracy of GP, the normalized root mean squared error (NRMSE) has been considered, given by

$$\text{NRMSE} = \sqrt{\sum(\hat{\Omega} - \Omega)^2 / \sum \Omega^2} \tag{29}$$

where Ω represents the true response quantity (frequency) and $\hat{\Omega}$ represents the predicted response quantity (frequency).

Convergence of the NRMSE in approximating the bandgap has been conducted to determine a suitable sample size for training the GP model as illustrated in Fig. 5. Moreover, the convergence study has been performed for various covariance functions of the GP model to assess their performance. Six well-known stationary covariance functions with full hyperparameter optimization have been investigated namely, Gaussian, exponential, linear, cubic, spherical and spline. Their functional forms have been illustrated in Appendix. For assessing the effect of pseudo random seeds used to generate the LHS samples on the error, the error bars along with the mean error have been presented corresponding to 50 seeds for each covariance function in Fig. 5. The error is observed to decrease with increasing sample size, illustrating monotonic convergence of the GP model. Based on the error bound and mean error for bandgap width below 5% and 2%, obtained respectively, in Fig. 5(b), the sample size of 50 has been selected for training the GP model in the subsequent analysis. It can be observed that all the covariance functions achieved nearly identical predictive accuracy after optimization of their hyperparameters. This highlights robust model performance across the covariance functions illustrating the fact that with sufficient data and proper optimization of their hyperparameters, the covariance functions effectively learn the characteristic length-scale of the function being approximated (frequency response, in our case).

Furthermore, to justify the choice of 5000 MCS samples for benchmarking the model predictive results, convergence of the NRMSE in approximating the bandgap has been carried out with training sample size for varying number of MCS samples up to 25,000 as illustrated in

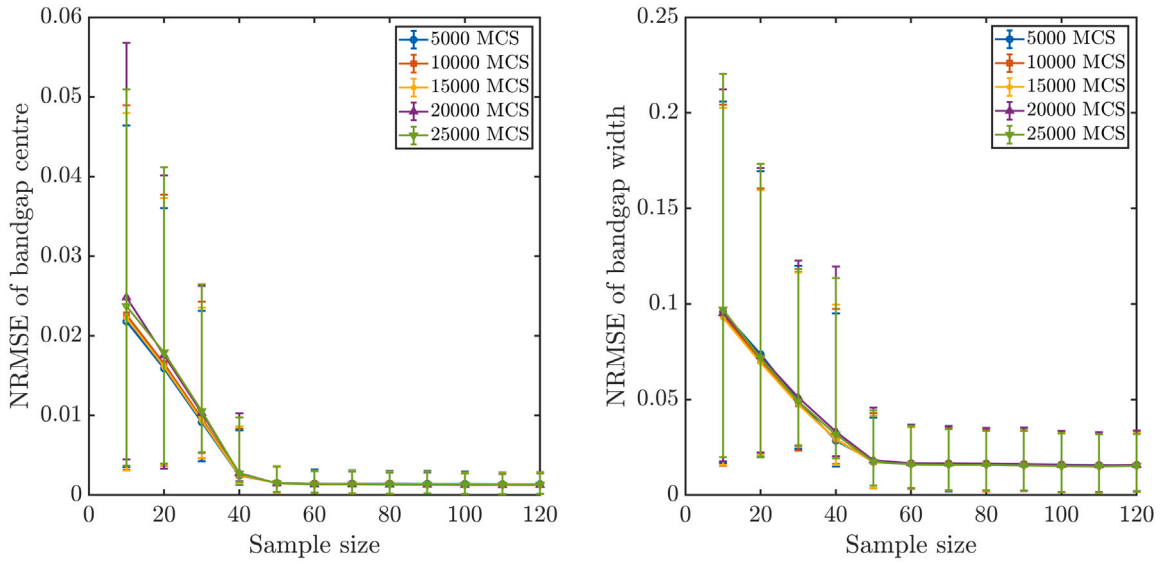

(a) Error convergence of the bandgap centre

(b) Error convergence of the bandgap width

Fig. 6. Convergence of the normalized root mean squared error with training sample size for varying number of Monte Carlo simulations in approximating the (a) bandgap center and (b) bandgap width. Note that the error bars have been obtained corresponding to the GP models trained on 50 different pseudo random seeds with the symbols representing the mean error values for the same number of MCS samples.

Fig. 6. Similar to Fig. 5, the error bars in Fig. 6 have been obtained across 50 pseudo random seeds for generating the LHS samples. It can be observed from the variation of the error bars that the effect of the number of MCS samples on the approximation error reduces with increase in the training sample size and only has a nominal effect from the sample size of 50 onwards. Since the GP model employed trained with 50 samples has been considered in this study, 5000 MCS samples should provide a satisfactory representation of the stochastic variation and validation of the GP approximation.

The stochastic variation in the wave dispersion behavior has been presented in Fig. 7. It can be observed from the maximum/minimum envelope and 95% confidence interval that there is significant variation in the frequency response due to variability within the unit cell. It should be noted that a bandgap is obtained for every stochastic realization as confirmed by the positive mean bandgap width in Table 1. This observation is explicitly stated as it may not be directly apparent from the stochastic dispersion plots in Fig. 7 where no bandgap could be represented due to the overlap of extreme statistical response variation resulting from different random realizations.

6.2. Multi-objective optimal design of the metamaterial nanobeam

A bi-objective optimization problem statement has been framed as stated in Eq. (30) to obtain the most desirable set of design variables within the unit cell corresponding to the specified objectives of (i) maximizing the bandgap width and (ii) minimizing the bandgap center. The design variables considered in the formulation based on the previous stochastic analysis include, material parameters, the elastic modulus (E), density (ρ), geometry parameters, radius (r), unit cell length (a), and the resonator stiffness (k_r). Note that the nonlocal and strain gradient parameters are not considered as the design variables for optimization due to their low contribution towards the objectives, i.e. bandgap center and width, as revealed from the stochastic analysis (see Fig. 4 and Table 1). Thus, the previously conducted stochastic response analysis scientifically informs and justifies the formulation of the optimization problem statement. Hence the optimization problem is,

$$
\begin{aligned}
&\textbf{Minimize}: \quad \text{Bandgap center},\\
&\textbf{Maximize}: \quad \text{Bandgap width},\\
&\textbf{To obtain}: \quad E, \rho, r, a \text{ and } k_r,\\
&\textbf{where}:\\
&\quad 67 \le E \le 73 \text{ (in GPa)},\\
&\quad 2600 \le \rho \le 2800 \text{ (in kg/m}^3\text{)},\\
&\quad 0.45\times10^{-9} \le r \le 0.55\times10^{-9} \text{ (in m)},\\
&\quad 18r \le a \le 22r \text{ (in m)},\\
&\quad (1.6274\pi\times10^8)^2 m_r \le k_r \le (2.2878\pi\times10^8)^2 m_r \text{ (in N/m)}.
\end{aligned}
\tag{30}
$$

To solve the optimization problem, the well-known evolutionary algorithm, the non-dominated classification genetic algorithm II (NSGA-II), has been used [85]. NSGA-II is a gradient-free global optimization technique capable of yielding solutions to complex problems. To implement NSGA-II, the built-in MATLAB toolbox 'gamultiobj' has been employed for this work. The total number of population and generations considered in the optimization is 100 and 100, respectively. All other evolutionary parameters in the toolbox were kept as their default values.

The results of the multi-objective optimization problem have been presented in Fig. 8 in the form of a Pareto plot, where the two objectives are given on the two axes. The dispersion responses are presented alongside the Pareto front, corresponding to seven optimal solutions, for illustrative purposes. All of the 35 Pareto solution points illustrated have been numbered to track the corresponding dispersion plots shown alongside.

The Pareto front obtained by the actual simulation and the GP model trained offline on 50 samples using Gaussian covariance function are represented in Fig. 9. Note that offline training implies that the GP is trained once prior to the optimization process and is subsequently used to predict the dispersion response during optimization iterations. For more details on offline surrogate model training and its integration with an evolutionary multi-objective optimization algorithm, one is referred to the proposed approach 1 of [86]. Consequently, no additional simulations are required during optimization, making the computational framework highly efficient.

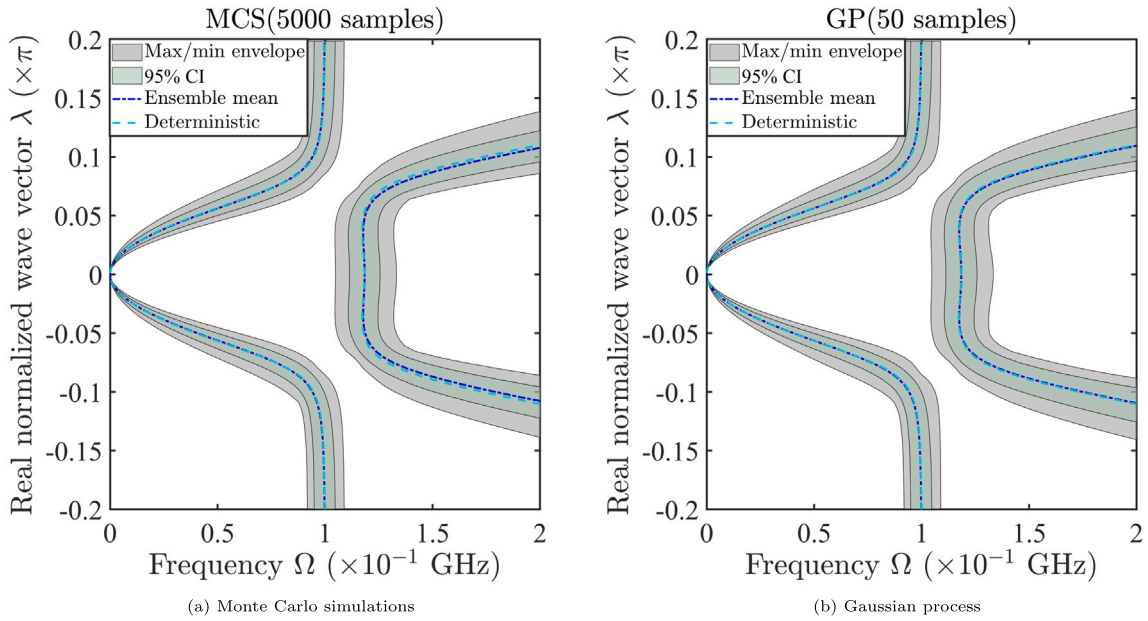

(a) Monte Carlo simulations (b) Gaussian process

Fig. 7. Stochastic dispersion plots obtained using (a) MCS (5000 samples) and (b) GP (50 samples) using Gaussian covariance.

The close proximity of the Pareto solutions demonstrates the accurate performance of the offline-trained GP model. In order to further quantify the accuracy, the performance metrics: generational distance (GD) and inverted generational distance (IGD) have been evaluated. Both GD and IGD measure the convergence towards the optimal Pareto front and hence, a lower value is considered to be better [87].

Remark 1. The performance metric GD computes the average distance between each element a_i of a Pareto front approximation (in this case, objectives obtained by GP) and its nearest reference point in Z, and is given by

$$\mathrm{GD}(A) = \frac{1}{|A|}\left(\sum_{i=1}^{|A|}\min_{j=1}^{|Z|}\|a_i - z_j\|^p\right)^{1/p} \tag{31}$$

where $A = \{\boldsymbol{a}_1, \boldsymbol{a}_2, \ldots, \boldsymbol{a}_{|A|}\}$ forms the entries of the approximate Pareto front, $Z = \{\boldsymbol{z}_1, \boldsymbol{z}_2, \ldots, \boldsymbol{z}_{|Z|}\}$ are the entries of the reference set, $|A|$ denotes the cardinality of A, $|Z|$ denotes the cardinality of Z and $p = 2$ to measure the Euclidean distance (2-norm).

Remark 2. The performance metric IGD computes the average distance between each element z_i of the reference set from its nearest point in the Pareto front approximation A, and is given by

$$\mathrm{IGD}(Z) = \frac{1}{|Z|}\left(\sum_{i=1}^{|Z|}\min_{j=1}^{|A|}\|z_i - a_j\|^p\right)^{1/p} \tag{32}$$

In the absence of a reference point set, Z is considered to be the actual objective vector set. Based on the Pareto optimal solutions in Fig. 9, the GD and IGD metrics are calculated as, 6.63×10^{-4} and 4.91×10^{-4}, respectively, which are 2–3 orders of magnitude lower than the best objective function values, thus, illustrating satisfactory convergence of the Pareto front by GP relative to that obtained from the actual simulation.

7. Conclusion

This work presents a first-of-its-kind investigation of stochastic dispersion and design optimization of locally resonant nanobeam metamaterials using nonlocal strain gradient theory. By quantifying geometric, material, and scale-dependent randomness at the unit cell level, it is demonstrated that geometric variability induces the largest shifts in bandgap location and width, with material variability being secondary and scale effects negligible. Notably, the bandgap width is more sensitive than its location. Leveraging a Gaussian process (GP) surrogate, the proposed framework predicts stochastic dispersion with less than 2% normalized root mean squared error and enables multi-objective inverse design of metamaterial structures based on user-defined bandgap features without requiring repeated full-model simulations.

A key contribution of this study lies in the generalizability of the proposed computational framework. By combining length-scale and uncertainty-aware dispersion modeling with a machine learning-driven optimization pipeline, the methodology is transferable to a wide range of metamaterial nanostructures beyond nanobeams. For clarity and broader impact, the extensible features of the computational workflow are categorized across four key modules:

(i) **Dispersion Modeling of Metamaterial Nanostructures:**

- The framework can be adapted to study the dispersion characteristics of other periodic nanostructural configurations, such as nanoplates and shell lattices, by incorporating size-dependent effects using nonlocal and strain gradient parameters for assessing the technology readiness of next-generation nano-metastructures.
- Within the same pipeline, users can rapidly explore how design variations such as changes in unit cell geometry, material classes, and internal resonator configurations affect bandgap emergence across a broad class of elastic metamaterials.
- The bandgap formation analysis is flexible to incorporate alternative approaches, such as the transfer matrix method and/or spectral element methods.

(ii) **Stochastic Computational Modeling:**

- Additional variability in modeling parameters, otherwise assumed deterministic, such as the mass of internal resonators, can be seamlessly introduced.
- Known correlations between random parameters can be readily implemented.

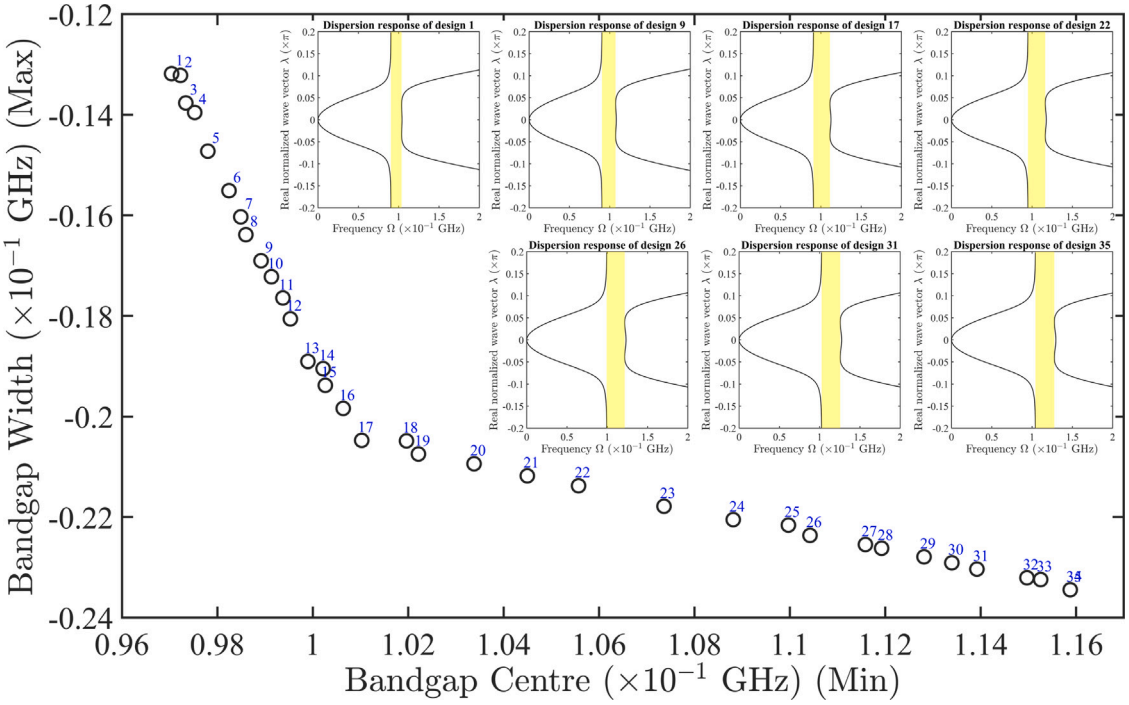

Fig. 8. The resulting Pareto front based on the multi-objective optimal design obtained by the actual simulation. 35 points are indicated in the Pareto front (35% of the total population, where the total population is 100). Note that the negative sign on the y-axis result due to the maximization of the objective, essentially illustrating positive values of bandgap width. The dispersion response corresponding to seven optimal design configurations have been presented for representative purposes. For the purpose of correlating the Pareto solutions with the representative dispersion response plots, these have been numbered.

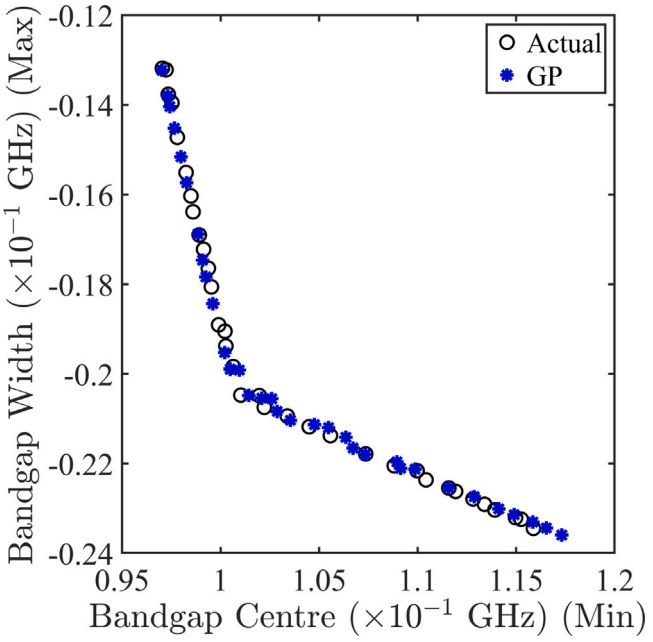

Fig. 9. The resulting Pareto front based on the multi-objective optimal design obtained by the actual simulation and GP model. The GP model is trained on 50 samples. 35 points are indicated in the Pareto front (35% of the total population, where the total population is 100). Note that the negative sign on the y-axis result due to the maximization of the objective, essentially illustrating positive values of bandgap width.

- Non-parametric stochastic modeling can be adopted depending on the level of available knowledge of the system parameters (see, e.g., [88]).

(iii) **Machine Learning Surrogate:**

- The approach is non-intrusive and can thus be generalized to other predictive modeling and optimization tasks with minimal changes.
- It can quantify predictive uncertainty due to the Bayesian nature of the GP.
- It accommodates arbitrary probabilistic distributions of stochastic input parameters.
- The surrogate model can be trained using alternative sampling or training schemes.
- It is compatible with enhancements to GP or integration with other machine learning or deep learning models.

(iv) **Design Optimization:**

- The optimization strategy is modular and agnostic to the choice of optimization algorithm.
- It can incorporate physical constraints and additional objectives to embed user preferences and support multi-criteria decision making.
- Modern AI-based generative models and reinforcement learning tools can be integrated for inverse design.

These extensible features equip designers with fast, uncertainty-aware, customizable tools for broader multifunctional applications in nanomechanics, nanophononics, nanoscale waveguiding, wave filtering, acoustic sensing, and energy harvesting. Future work will consider extending spatially varying uncertainties beyond the unit cell to full metastructures. This will enable the modeling of defect-induced effects and capture the propagation of stochastic behavior at the global scale. Such an enhancement, combined with reliability-based and robust optimization, promises scalable and efficient metamaterial design under uncertainty.

CRediT authorship contribution statement

T. Chatterjee: Writing – original draft, Validation, Software, Methodology, Investigation. **S. El-Borgi:** Writing – review & editing, Supervision, Project administration, Methodology, Conceptualization. **M. Trabelssi:** Writing – review & editing, Supervision. **M.I. Friswell:** Writing – original draft, Investigation, Conceptualization.

Declaration of competing interest

The authors declare that they have no known competing financial interests or personal relationships that could have appeared to influence the work reported in this paper.

Acknowledgments

The first author gratefully acknowledges the support of the University of Surrey through the award of a faculty start-up grant.

Appendix. Correlation functions for the gp model

The correlation function used for the GP model can be expressed as products of stationary, one-dimensional correlations,

$$\mathbf{R}(\theta, \mathbf{x}, \mathbf{x}') = \prod_{j=1}^{d} R_j(\theta_j, x_j, x_j') \tag{33}$$

The six different correlation functions considered in this study are:

1. **Exponential**

$$R_j(\theta_j, x_j, x_j') = \exp(-\theta_j |x_j - x_j'|) \tag{34}$$

2. **Gaussian**

$$R_j(\theta_j, x_j, x_j') = \exp(-\theta_j (x_j - x_j')^2) \tag{35}$$

3. **Linear**

$$R_j(\theta_j, x_j, x_j') = \max(0, 1 - \theta_j |x_j - x_j'|) \tag{36}$$

4. **Spherical**

$$R_j(\theta_j, x_j, x_j') = 1 - 1.5\zeta_j + 0.5\zeta_j^3, \quad \text{where } \zeta_j = \min(1, \theta_j |x_j - x_j'|) \tag{37}$$

5. **Cubic**

$$R_j(\theta_j, x_j, x_j') = 1 - 3\zeta_j^2 + 2\zeta_j^3, \quad \text{where } \zeta_j = \min(1, \theta_j |x_j - x_j'|) \tag{38}$$

6. **Spline**

$$R_j(\theta_j, x_j, x_j') = \begin{cases} 1 - 15\zeta_j^2 + 30\zeta_j^3, & 0 \le \zeta_j \le 0.2 \\ 1.25(1 - \zeta_j)^3, & 0.2 < \zeta_j \le 1 \\ 0, & \zeta_j > 1, \end{cases} \quad \text{where } \zeta_j = \theta_j |x_j - x_j'| \tag{39}$$

It is to be noted that in all cases the correlation decreases with increasing $|x_j - x_j'|$ and a larger value of θ_j results in a more rapid decay. The correlation functions listed above can be categorized into two groups: those exhibiting parabolic behavior near the origin such as the Gaussian, cubic, and spline functions and those with linear behavior near the origin including the exponential, linear, and spherical functions.

The selection of an appropriate correlation function should be guided by the characteristics of the underlying phenomenon, such as the nature of the objective function or the physical process being modeled. For processes that are continuously differentiable, correlation functions with parabolic behavior near the origin (e.g., Gaussian, cubic, spline) are generally more suitable. In contrast, physical phenomena often exhibit linear behavior near the origin, making exponential, linear, or spherical functions preferable. For large distances, the linear, cubic, spherical, and spline functions lead to zero correlation beyond a certain threshold, whereas the exponential and Gaussian types decay asymptotically to zero [80].

In many practical cases, the phenomenon under study is anisotropic exhibiting different correlation characteristics along different spatial directions. This directional variability is accommodated in the correlation model by allowing distinct parameters θ_j for each of the d dimensions.

Data availability

The results in this paper are simulated based on a numerical model that is detailed in the paper. The parameters used for the simulations are stated in the paper, and so sufficient information is given for the reported results to be reproduced.

References

[1] B. Assouar, M. Oudich, X. Zhou, Acoustic metamaterials for sound mitigation, C. R. Phys. 17 (2016) 524–532.
[2] Z.C. He, X. Xiao, E. Li, Design for structural vibration suppression in laminate acoustic metamaterials, Compos. Part B: Eng. 131 (2017) 237–252.
[3] S. Brûlé, S. Enoch, S. Guenneau, Emergence of seismic metamaterials: Current state and future perspectives, Phys. Lett. A 384 (1) (2020) 126034.
[4] M. Jaberzadeh, B. Li, K.T. Tan, Wave propagation in an elastic metamaterial with anisotropic effective mass density, Wave Motion 89 (2019) 131–141.
[5] Z. Du, H. Chen, G. Huang, Optimal quantum valley hall insulators by rationally engineering berry curvature and band structure, J. Mech. Phys. Solids 135 (2020) 103784.
[6] S.S.R. Kumar, V.K. Krishnadas, K. Balasubramaniam, P. Rajagopal, Waveguide metamaterial rod as mechanical acoustic filter for enhancing nonlinear ultrasonic detection, APL Mater. 9 (2021) 061115.
[7] G. Zhao, S. Bi, M. Niu, Y. Cui, A zero refraction metamaterial and its application in electromagnetic stealth cloak, Mater. Today Commun. 21 (2019) 100603.
[8] A.C. Eringen, D.G.B. Edelen, On nonlocal elasticity, Internat. J. Engrg. Sci. 10 (3) (1972) 233–248.
[9] A.C. Eringen, On differential equations of nonlocal elasticity and solutions of screw dislocation and surface waves, J. Appl. Phys. 54 (9) (1983) 4703–4710.
[10] A.C. Eringen, Nonlocal Continuum Field Theories, Springer New York, 2004.
[11] X. Zhu, L. Li, Closed form solution for a nonlocal strain gradient rod in tension, Internat. J. Engrg. Sci. 119 (2017) 16–28.
[12] M. Trabelssi, S. El-Borgi, L.-L. Ke, J.N. Reddy, Nonlocal free vibration of graded nanobeams resting on a nonlinear elastic foundation using DQM and LaDQM, Compos. Struct. 176 (2017) 736–747.
[13] Sami El-Borgi, Prakash Rajendran, Mohamed Trabelssi, Application of combined nonlocal and surface elasticity theories to vibration response of a graded nanobeam, Size-Depend. Contin. Mech. Approaches: Theory Appl. (2021) 223–260.
[14] S. El-Borgi, P. Rajendran, M. Trabelssi, Nonlocal and surface effects on nonlinear vibration response of a graded Timoshenko nanobeam, Arch. Appl. Mech. 93 (1) (2023) 151–180.
[15] M. Trabelssi, S. El-Borgi, M.I. Friswell, A high-order FEM formulation for free and forced vibration analysis of a nonlocal nonlinear graded Timoshenko nanobeam based on the weak form quadrature element method, Arch. Appl. Mech. 90 (2020) 2133–2156.
[16] R.D. Mindlin, Micro-structure in linear elasticity, Arch. Ration. Mech. Anal. 16 (1) (1964) 51–78.
[17] E.C. Aifantis, On the role of gradients in the localization of deformation and fracture, Internat. J. Engrg. Sci. 30 (1992) 1279–1299.
[18] F. Yang, A.C.M. Chong, D.C.C. Lam, P. Tong, Couple stress based strain gradient theory for elasticity, Int. J. Solids Struct. 39 (2002) 2731–2743.
[19] M. Trabelssi, S. El-Borgi, A novel formulation for the weak quadrature element method for solving vibration of strain gradient graded nonlinear nanobeams, Acta Mech. 233 (11) (2022) 4685–4709.
[20] Y. Tian, B. Xu, D. Yu, Y. Ma, Y. Wang, Y. Jiang, W. Hu, C. Tang, Y. Gao, K. Luo, Z. Zhao, L.M. Wang, B. Wen, J. He, Z. Liu, Ultrahard nanotwinned cubic boron nitride, Nature 493 (2013) 385–388.
[21] C.W. Lim, G. Zhang, J.N. Reddy, A higher-order nonlocal elasticity and strain gradient theory and its applications in wave propagation, J. Mech. Phys. Solids 78 (2015) 298–313.

[22] S. El-Borgi, P. Rajendran, M.I. Friswell, M. Trabelssi, J.N. Reddy, Torsional vibration of size-dependent viscoelastic rods using nonlocal strain and velocity gradient theory, Compos. Struct. 186 (2018) 274–292.
[23] L. Li, Y. Hu, X. Li, Longitudinal vibration of size-dependent rods via nonlocal strain gradient theory, Int. J. Mech. Sci. 115–116 (2016) 135–144.
[24] L. Li, Y. Hu, Nonlinear bending and free vibration analyses of nonlocal strain gradient beams made of functionally graded material, Internat. J. Engrg. Sci. 107 (2016) 77–97.
[25] L. Li, Y. Hu, Wave propagation in fluid-conveying viscoelastic carbon nanotubes based on nonlocal strain gradient theory, Comput. Mater. Sci. 112 (2016) 282–288.
[26] X. Li, L. Li, Y. Hu, Z. Ding, W. Deng, Bending, buckling and vibration of axially functionally graded beams based on nonlocal strain gradient theory, Compos. Struct. 165 (2017) 250–265.
[27] M.R. Barati, A. Zenkour, A general bi-Helmholtz nonlocal strain-gradient elasticity for wave propagation in nanoporous graded double-nanobeam systems on elastic substrate, Compos. Struct. 168 (2017) 885–892.
[28] H.M. Ouakad, S. El-Borgi, S.M. Mousavi, M.I. Friswell, Static and dynamic response of CNT nanobeam using nonlocal strain and velocity gradient theory, Appl. Math. Model. 62 (2018) 207–222.
[29] F. Ebrahimi, M.R. Barati, A. Dabbagh, A nonlocal strain gradient theory for wave propagation analysis in temperature-dependent inhomogeneous nanoplates, Internat. J. Engrg. Sci. 107 (2016) 169–182.
[30] F. Ebrahimi, A. Dabbagh, On flexural wave propagation responses of smart FG magneto-electro-elastic nanoplates via nonlocal strain gradient theory, Compos. Struct. 162 (2017) 281–293.
[31] N. Challamel, S. El-Borgi, M. Trabelssi, J.N. Reddy, Buckling of micromorphic Timoshenko columns, Eur. J. Mech. A Solids (2024) 105537.
[32] N. Challamel, S. El-Borgi, M. Trabelssi, J.N. Reddy, Free vibration response of micromorphic Timoshenko beams, J. Sound Vib. 591 (2024) 118602.
[33] M. Trabelssi, S. El-Borgi, Vibration of nonlocal strain gradient functionally graded nonlinear nanobeams using a novel locally adaptive strong quadrature element method, Proc. Inst. Mech. Eng. Part N: J. Nanomater. Nanoeng. Nanosyst. (2022) 23977914221129426.
[34] L. Lu, X. Guo, J. Zhao, A unified size-dependent plate model based on nonlocal strain gradient theory including surface effects, Appl. Math. Model. 68 (2019) 583–602.
[35] D. Qian, Z. Shi, C. Ning, J. Wang, Nonlinear bandgap properties in a nonlocal piezoelectric phononic crystal nanobeam, Phys. Lett. A 383 (25) (2019) 3101–3107.
[36] W. Zhou, W. Chen, C.W. Lim, Surface effect on the propagation of flexural waves in periodic nano-beam and the size-dependent topological properties, Compos. Struct. 216 (2019) 427–435.
[37] D. Qian, J. Wu, F. He, Electro-mechanical coupling band gaps of a piezoelectric phononic crystal Timoshenko nanobeam with surface effects, Ultrasonics 109 (2021) 106225.
[38] D. Qian, Electro-mechanical coupling wave propagating in a locally resonant piezoelectric/elastic phononic crystal nanobeam with surface effects, Appl. Math. Mech. 41 (3) (2020) 425–438.
[39] D. Qian, J. Wang, Studies of a new-style resonator to control electro-mechanical coupling bandgap of a locally resonant piezoelectric/elastic phononic crystal double-layer nonlocal nanobeam, Appl. Math. Model. 102 (2022) 786–796.
[40] M. Espo, S.M. Hosseini, M.H. Abolbashari, Bandgap characteristics of a piezoelectric phononic crystal Timoshenko nanobeam based on the modified couple stress and surface energy theories, Mater. Today Commun. 33 (2022) 104782.
[41] M. Trabelssi, S. El-Borgi, M.I. Friswell, Application of nonlocal strain gradient theory for the analysis of bandgap formation in metamaterial nanobeams, Appl. Math. Model. 127 (2024) 281–296.
[42] M. Schiantella, F. Cluni, V. Gusella, Geometrical uncertainties influence on the failure load estimation of lattice structures, Probabilistic Eng. Mech. 76 (2024) 103636.
[43] A. Krishnan, E. Dujardin, T.W. Ebbesen, P.N. Yianilos, M.M.J. Treacy, Young's modulus of single-walled nanotubes, Phys. Rev. B 58 (1998) 14013–14019.
[44] J.P. Salvetat, A.D. Briggs, J.M. Bonard, R.R. Bacsa, A.J. Kulik, T. Stöckli, N.A. Burnham, L. Forró, Elastic and shear moduli of single-walled carbon nanotube ropes, Phys. Rev. Lett. 82 (1999) 944–947.
[45] L. He, S. Guo, J. Lei, Z. Sha, Z. Liu, The effect of Stone Thrower Wales defects on mechanical properties of graphene sheets - A molecular dynamics study, Carbon 75 (2014) 124–132.
[46] H. Liu, Z. Lv, Vibration performance evaluation of smart magneto-electro-elastic nanobeam with consideration of nanomaterial uncertainties, J. Intell. Mater. Syst. Struct. 30 (18–19) (2019) 2932–2952.
[47] M.J. Mahmoodi, M. Khamehchi, Random distribution of interphase characteristics on the overall electro-mechanical properties of CNT piezo nanocomposite: Micromechanical modeling and Monte Carlo simulation, Probabilistic Eng. Mech. 75 (2024) 103577.
[48] E. Garcia-Macias, R. Castro-Triguero, M.I. Friswell, S. Adhikari, A. Saez, Metamodel-based approach for stochastic free vibration analysis of functionally graded carbon nanotube reinforced plates, Compos. Struct. 152 (2016) 183–198.
[49] T.-P. Chang, Nonlinear vibration of single-walled carbon nanotubes with nonlinear damping and random material properties under magnetic field, Compos. Part B: Eng. 114 (2017) 69–79.
[50] Z. Lv, H. Liu, Nonlinear bending response of functionally graded nanobeams with material uncertainties, Int. J. Mech. Sci. 134 (2017) 123–135.
[51] H. Ghasemi, R. Rafiee, X. Zhuang, J. Muthu, T. Rabczuk, Uncertainties propagation in metamodel-based probabilistic optimization of CNT/polymer composite structure using stochastic multi-scale modeling, Comput. Mater. Sci. 85 (2014) 295–305.
[52] S.K. Jena, S. Pradyumna, S. Chakraverty, Quantifying uncertainty in free vibration characteristics of nanobeam with one variable first-order shear deformation theory: an analytical investigation, Acta Mech. (2024) DOI: https://doi.org/10.1007/s00707-024-03955-6.
[53] A.T. Fabro, H. Meng, D. Chronopoulos, Uncertainties in the attenuation performance of a multi-frequency metastructure from additive manufacturing, Mech. Syst. Signal Process. 138 (2020) 106557.
[54] M. Schevenels, B.S. Lazarov, O. Sigmund, Robust topology optimization accounting for spatially varying manufacturing errors, Comput. Methods Appl. Mech. Engrg. 200 (49) (2011) 3613–3627.
[55] P. Celli, B. Yousefzadeh, C. Daraio, S. Gonella, Bandgap widening by disorder in rainbow metamaterials, Appl. Phys. Lett. 114 (2019) 091903.
[56] Z.C. He, J.Y. Hu, E. Li, An uncertainty model of acoustic metamaterials with random parameters, Comput. Mech. 62 (2018) 1023–1036.
[57] D. Beli, A.T. Fabro, M. Ruzzene, Jose Roberto F. Arruda, Wave attenuation and trapping in 3D printed cantilever-in-mass metamaterials with spatially correlated variability, Sci. Rep. 9 (2019) 5617.
[58] H.A. Babaa, S. Nandi, T. Singh, M. Nouh, Uncertainty quantification of tunable elastic metamaterials using polynomial chaos, J. Appl. Phys. 127 (2020) 015102.
[59] J. Henneberg, J.S. Gomez Nieto, K. Sepahvand, A. Gerlach, H. Cebulla, S. Marburg, Periodically arranged acoustic metamaterial in industrial applications: The need for uncertainty quantification, Appl. Acoust. 157 (2020) 107026.
[60] T. Chatterjee, D. Karlicic, S. Adhikari, M.I. Friswell, Gaussian process assisted stochastic dynamic analysis with applications to near-periodic structures, Mech. Syst. Signal Process. 149 (2021) 107218.
[61] T. Chatterjee, D. Karlicic, S. Adhikari, M.I. Friswell, Wave propagation in randomly parameterized 2D lattices via machine learning, Compos. Struct. 275 (2021) 114386.
[62] T. Chatterjee, D. Karlicic, M. Cajic, S. Adhikari, M.I. Friswell, Uncertainty quantification in inerter-based quasiperiodic lattices, Int. J. Mech. Sci. 249 (2023) 108258.
[63] T. Chatterjee, K.K. Bera, A. Banerjee, Machine learning enabled quantification of stochastic active metadamping in acoustic metamaterials, J. Sound Vib. 567 (2023) 117938.
[64] Kai Zhou, Zequn Wang, Qingbin Gao, Sichen Yuan, Jiong Tang, Recent advances in uncertainty quantification in structural response characterization and system identification, Probabilistic Eng. Mech. 74 (2023) 103507.
[65] Y.Y. Kim, Elastic Waves and Metamaterials: The Fundamentals, Springer, 2023.
[66] L. Li, Y. Hu, X. Li, Longitudinal vibration of size-dependent rods via nonlocal strain gradient theory, Int. J. Mech. Sci. 115 (2016) 135–144.
[67] J.N. Reddy, Theories and Analyses of Beams and Axisymmetric Circular Plates, CRC Press, 2022.
[68] D.J. Mead, Free wave propagation in periodically supported, infinite beams, J. Sound Vib. 11 (2) (1970) 181–197.
[69] D. Yu, Y. Liu, G. Wang, H. Zhao, J. Qiu, Flexural vibration band gaps in Timoshenko beams with locally resonant structures, J. Appl. Phys. 100 (12) (2006) 124901.
[70] L. Liu, M.I. Hussein, Wave motion in periodic flexural beams and characterization of the transition between Bragg scattering and local resonance, J. Appl. Mech. 79 (1) (2012).
[71] Y. Liu, D. Yu, L. Li, H. Zhao, J. Wen, X. Wen, Design guidelines for flexural wave attenuation of slender beams with local resonators, Phys. Lett. A 362 (5–6) (2007) 344–347.
[72] Y. Xiao, J. Wen, D. Yu, X. Wen, Flexural wave propagation in beams with periodically attached vibration absorbers: Band-gap behavior and band formation mechanisms, J. Sound Vib. 332 (4) (2013) 867–893.
[73] Y. Xiao, J. Wen, Closed-form formulas for bandgap estimation and design of metastructures undergoing longitudinal or torsional vibration, J. Sound Vib. 485 (2020) 115578.
[74] H. Sun, X. Du, P.F. Pai, Theory of metamaterial beams for broadband vibration absorption, J. Intell. Mater. Syst. Struct. 21 (11) (2010) 1085–1101.
[75] T. Wang, M.-P. Sheng, Q.-H. Qin, Multi-flexural band gaps in an Euler–Bernoulli beam with lateral local resonators, Phys. Lett. A 380 (4) (2016) 525–529.
[76] C.E. Rasmussen, C.K.I. Williams, Gaussian Processes for Machine Learning, The MIT Press, Cambridge, Massachusetts London, England, ISBN: 026218253X, 2006.
[77] B. Sudret, Meta-models for structural reliability and uncertainty quantification, in: Proceedings of 5th Asian-Pacific Symposium on Stuctural Reliabilty and Its Applications (APSSRA, 2012), Singapore, 2012, pp. 53–76.
[78] D.G. Krige, A Statistical approach to some basic mine valuation problems on the witwatersrand, J. Chem. Met. Min. Soc. South Afr. 52 (6) (1951) 119–139.

[79] T. Chatterjee, S. Adhikari, M.I. Friswell, Uncertainty propagation in dynamic sub-structuring by model reduction integrated domain decomposition, Comput. Methods Appl. Mech. Engrg. 366 (2020) 113060.
[80] S.N. Lophaven, H.B. Nielson, J. Sondergaard, DACE A MATLAB Kriging Toolbox, Technical report, IMM-TR-2002-12, Technical University of Denmark, Technical University of Denmark, 2002.
[81] T. Chatterjee, R. Chowdhury, Hp adaptive model based approximation of moment free sensitivity indices, Comput. Methods Appl. Mech. Engrg. 332 (2018) 572–599.
[82] T. Chatterjee, R. Chowdhury, Refined sparse Bayesian learning configuration for stochastic response analysis, Probabilistic Eng. Mech. 52 (2018) 15–27.
[83] T. Chatterjee, R. Chowdhury, Adaptive bilevel approximation technique for multiobjective evolutionary optimization, J. Comput. Civ. Eng. 31 (3) (2017) 04016071.
[84] A.N.O. Connor, M. Modarres, A. Mosleh, Probability Distributions Used in Reliability Engineering, The Center for Risk and Reliability, University of Maryland, ISBN: 978-0-9966468-1-9, 2016.
[85] K. Deb, A. Pratap, S. Agarwal, T. Meyarivan, A fast and elitist multiobjective genetic algorithm: NSGA-II, IEEE Trans. Evol. Comput. 6 (2) (2002) 182–197.
[86] T. Chatterjee, R. Chowdhury, Adaptive bilevel approximation technique for multiobjective evolutionary optimization, J. Comput. Civ. Eng. 31 (3) (2017) 04016071.
[87] C. Audet, J. Bigeon, D. Cartier, S. Le Digabel, L. Salomon, Performance indicators in multiobjective optimization, European J. Oper. Res. 292 (2) (2021) 397–422.
[88] T. Chatterjee, S. Adhikari, M.I. Friswell, H.H. Khodaparast, Non-parametric stochastic reduced-order modelling of built-up structures, in: Proceedings of the 9th International Conference on Uncertainty in Structural Dynamics, USD 2022, KU Leuven, Belgium, 2022.